# A Probe Antenna for *In Situ* Measurement of the Complex Dielectric Constant of Materials

Elias M. Nassar, *Member, IEEE*, Robert Lee, *Member, IEEE*, and Jonathan D. Young, *Fellow, IEEE*

***Abstract*—A new probe for the *in situ* measurement of the complex dielectric constant of materials in the microwave frequency region is described. The probe uses two stub antennas mounted on a cylinder. The cylinder is inserted in the material and the transmission coefficient between the two antennas is measured. By comparing this signal with that predicted from a numerical model of the probe obtained by the finite-difference time-domain (FDTD) method we can determine the dielectric constant of the material. The measurement setup and numerical model of the probe are described and several measurement examples in natural and artificial media are presented.**

***Index Terms*—Dielectric measurements, probe antennas.**

## I. Introduction

THE use of electromagnetic waves for the measurement of the complex dielectric constant of materials has been previously studied [1]. In many cases, there is a need to measure the complex dielectric constant *in situ* so as not to modify properties of the material by the extraction, cutting, and transportation of the sample, which are necessary in laboratory-type measurements [2]. Also, in remote sensing and ground-penetrating radar applications it is often desirable to know the dielectric constant profile versus depth for a wide band of frequencies since the electromagnetic scattering is strongly dependent on the material profile. Without an accurate characterization of the material profile it becomes very difficult to develop a good inverse scattering model.

*In situ* methods are generally divided into two categories—surface and drill-hole measurement techniques [3]. Surface techniques are used whenever a drill hole is not feasible or when dielectric constant values are needed over very large areas. Drill-hole techniques, on the other hand, are usually used to get localized values of dielectric constant and to measure depth profiles in the material. Earlier drill-hole type probes for soil measurements have been limited to frequencies below 1 GHz [4].

In this study, we develop a new hand-held, ultrawide-band drill-hole-type probe antenna for the *in situ* measurement of the complex dielectric constant. This probe uses two stub antennas [5] mounted on a copper cylinder (Fig. 1). To perform a measurement, the probe is inserted in the material under study. Then a signal is transmitted by one of the antennas and received by the other. Based on the comparison of the received signal to the predicted signal from a numerical model of the probe antenna, we can extract the complex dielectric constant.

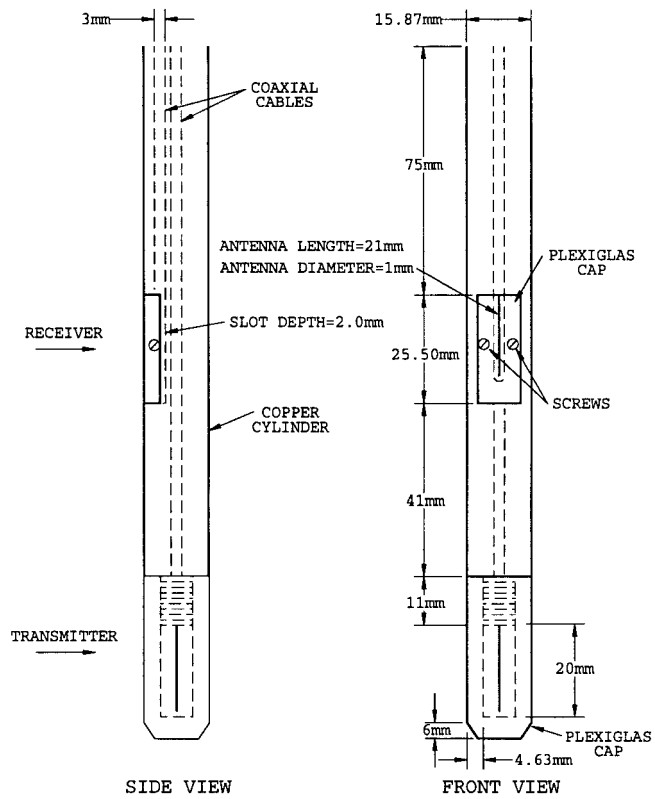


Fig. 1. Front and side views of the electromagnetic probe showing the coaxial cables in the copper cylinder, the antennas, and plexiglass covers.

The geometry of the probe antenna is shown in Fig. 1. Although the two stub antennas have very low gain, the outer surface of the copper cylinder acts as a guiding structure, so that the coupling between the two antennas is very strong. This coupling is dependent upon the properties of the material in which the probe is immersed. If an accurate electromagnetic model can be obtained for the probe interaction with the material, we can accurately extract the complex dielectric constant of the material. A simple plane wave approximation for the wave traveling between the two antennas might be considered. This approximation is fairly accurate because the guided wave along the surface of the copper cylinder can be considered to be quasi-TEM. There are several factors that may cause differences from this ideal model. The plane wave model does not account for the input impedance and pattern of the antennas. Furthermore, there may be reflections at the

Manuscript received October 10, 1996; revised March 24, 1999. This work was supported by the Office of Naval Research under Contract N00014-92-J-1791 and by the Joint Services Electronics Program under Contract N00014-89-J-1007.

The authors are with the ElectroScience Laboratory, Department of Electrical Engineering, The Ohio State University, Columbus, OH 43212 USA.

Publisher Item Identifier S 0018-926X(99)05822-6.

0018–926X/99$10.00 © 1999 IEEE

antenna/material interface. An alternative model is obtained from the finite-difference time-domain (FDTD) method, which should produce a more accurate solution than the first method, but is more computationally expensive to obtain.

Section II of this paper deals with the design of the probe antenna while Section III describes the FDTD model of the antenna. In Section IV, we present a method for measuring the complex dielectric constant of any material using a lookup table. By comparing the measured data with the values in the table we will obtain dielectric constant values for materials such as nylon, soil, and sea ice. Finally, in Section V we draw some conclusions from this study.

## II. Antenna Dsign

### A. Antenna Geometry

A schematic diagram for the antenna is shown in Fig. 1. Two semi-rigid coaxial cables are inserted into a copper cylinder having the dimensions shown. One of the cables extends to the end of the cylinder and the other to a distance of 5 cm from the end. The outer conductor and dielectric on each of the cables' last 2 cm are stripped to expose the center conductors, which will be used as transmitting and receiving stub antennas. A 2.5-cm-long $\times$ 1-cm-wide opening is cut in the cylinder for the middle antenna and is then filled with a flat metal insert. The antenna is located in a semi-circular slot of radius 2 mm carved into the metal insert (see Fig. 4). The insert eliminates any internal coupling between the antennas through the inner part of the cylinder.

Both antennas are covered with plexiglass caps shaped to match the surface of the copper cylinder. These caps help to isolate them from the surrounding medium and to produce a smooth surface for the probe when it is inserted in the material under study; waterproofing is done at the interface between the caps and the cylinder's walls to prevent leaking of liquids into the antennas' cavities.

The probe is intended to operate in the range of frequencies from 2 to 10 GHz which matches the frequency range where radar backscatter measurements were performed. The minimum phase variation in the coupled signal occurs at the lowest frequency and the maximum attenuation occurs at the highest frequency. Also, the resolution in measuring dielectric constant profiles versus depth is determined by the antenna separation. To achieve a tradeoff between these three requirements, we chose an antenna separation of 7.6 cm that is equal to half a wavelength at 2 GHz in free-space.

Both antennas are 2 cm long or one eighth of a wavelength at 2 GHz; these antennas do not radiate very efficiently below 2 GHz and the coupling between the antennas is reduced considerably. The total length of the probe apparatus is 40 cm. This length can be varied based on the desired maximum measurement depth. A handle is soldered at the end of the probe to be used in insertion and retrieval of the probe from the material.

### B. Measurement Procedure

In order to perform a measurement, the probe is connected to a network analyzer which is controlled by a personal computer as shown in Fig. 2. The coaxial cable of the middle antenna is connected to the receiver and that of the tip antenna to the transmitter of the network analyzer which measures the coupled signal between the antennas ($S_{21}$). The network analyzer transmits a single-frequency signal that travels through the coaxial cable to the tip antenna. Part of this signal is reflected at the antenna terminal and part is radiated in the material around the probe. A fraction of the radiated signal is received by the middle antenna, detected by the network analyzer and recorded by the personal computer. This process is then repeated with the network analyzer stepping through the frequency range from 2 to 10 GHz in steps of 20 MHz.

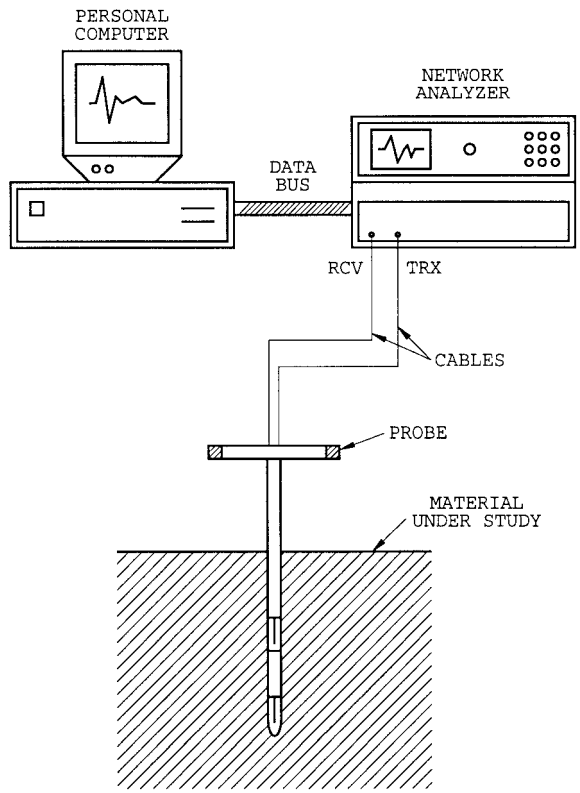


Fig. 2. Measurement setup for electromagnetic probe. The two coaxial cables are connected to the network analyzer ports and the measured signal is stored on the PC.

A first, measurement is taken in free-space to check the operation of the probe. This is done by recording three signals:

- the coupled signal between the antennas ($S_{21}$);
- the reflected signal from the tip antenna ($S_{11}$);
- the reflected signal from the middle antenna ($S_{22}$).

These signals indicate if any of the antennas or connections is not working properly before performing the material measurement.

A cylindrical hole of the same diameter as the probe is then drilled and the probe inserted in the material and a second measurement ($S_{21}$) is recorded with the probe in the material.

To a first level of approximation, medium parameters can be deduced from the $S_{21}$ measurement. The actual behavior with higher order mechanisms included is discussed later in this paper.

In order to minimize any measurement errors, care should be taken to eliminate any air gaps between the probe and the material walls. The probe should also be far enough from the boundaries of the sample in order to prevent the reflections at the boundaries from interfering with the direct signal between the transmitter and receiver. If these reflections are far enough in time from the direct coupled signal they can be gated out before the signal is processed to extract the complex dielectric constant.

## III. FDTD Model

In order to calibrate and interpret the measurements done with the probe, we develop a three-dimensional (3-D) numerical model using the FDTD technique. This method first proposed by Yee [9] has recently been used to model antennas [10]–[12]. In this study, we use the perfectly matched layer (PML) medium formulation introduced by Berenger [15] to simulate the radiation boundary condition.

### A. Parameters of FDTD Model

*1) Source and Receiver:* The coaxial cables are simulated using four cells in the $x$–$y$ plane backed by a perfect electric conductor, as shown in Fig. 4.

The center conductor of the coaxial cable is modeled with the integral-based formulation in [13]. The electric field in the $z$-direction $E_z$ is set to zero at the intersection of the four cells and a special updating expression is used for $H_x$ and $H_y$ located in the four cells of the coaxial cable.

The relative dielectric constant inside the coax is set to 2.6, which is the value of the real part of the dielectric constant of teflon, used in the probe cables.

The pulse shape of the excitation is a differentiated Gaussian given by the following expression:

$$V(n\Delta t) = \frac{(n\Delta t - \alpha T)}{T^2} e^{-((n\Delta t - \alpha T)/T)^2}. \tag{1}$$

The choice of the differential Gaussian pulse is motivated by the fact that it is desirable to minimize the dc content of the spectrum, which grows linearly with time during late-time computations. In the above expression, we set $\alpha = 3.0$, $T = 0.05/2c\alpha$, where $c$ is the speed of light in free-space and $\Delta t$ is the time step. The constants are chosen to ensure that the incident pulse propagating down the coaxial cable has decayed to zero at the source point before any reflections from the coax/antenna transition return to the source. This condition allows us to use the total field formulation in the coaxial cable. In order to excite the transmitter antenna we set the four TE fields in the coax to the value of the source pulse to simulate a TEM wave propagating in the coax (Fig. 4). The received signal is sampled inside the coax connected to the middle antenna. The expression used to compute the received voltage assumes a static field distribution in the coax [8]

$$V_r(n\Delta t) = E_x^{n\Delta t}(i, j, k)\frac{\Delta x}{2} \ln\left(\frac{\Delta x}{a}\right) \tag{2}$$

where $V_r$ is the received voltage, $a$ is the radius of the center conductor, and $\Delta x$ the space step.

*2) Antennas:* The two antennas are also modeled with the same thin-wire approximations used for the center conductor of the coaxial cables. The slot near the middle antenna is modeled using the half-cell formulation of [14].

The size of the slot proved to have a large effect on the antenna radiation pattern. By using different slot sizes, we were able to gain insight into how the design of the probe can be improved to achieve better coupling between the two antennas. The plexiglass caps around the antennas are modeled by setting the real part of the relative dielectric constant of the corresponding cells to 2.7; the conductivity for this material is $4 \times 10^{-4}$ Mho/m. A stair-step approximation is used for the circular cap surface.

*3) Copper Cylinder:* In order to model the circular conducting cylinder, we make use of the half-cell integral formulation as shown in Fig. 4. Since the size of the domain that can be meshed in FDTD is limited by the memory storage resources of the computer used for the simulation, we only mesh the part of the probe that contains the two antennas, i.e., the last 20 cm of the probe. This part is shown in Fig. 3. The remaining part of the probe including the handle does not have an effect on the transmission coefficient in the material except for reflections from the handle that can be gated out before processing the data. The effect of the cable length that connects the probe to the network analyzer can be eliminated by dividing the complex transmission coefficient ($S_{21}$) in the material by that in free-space. The cylinder extends into the PML which absorbs any reflections from the truncated edge of the cylinder.

Each of the conducting screws holding the middle cap to the cylinder is modeled by one FDTD cell in which the electric field is set to zero.

*4) Absorbing Boundary Condition:* The space around the probe is terminated by the PML absorbing boundary condition (PML ABC) introduced by Berenger [15]. This type of ABC gives very low levels of reflection at the boundary by employing a lossy material that is matched to the material in the computation space in the three Cartesian coordinate directions. In order to achieve this absorption the six electric and magnetic field components are split in two as shown below for $E_x$ and $H_y$

$$E_x = E_y^x + E_z^x \tag{3}$$
$$H_y = H_x^y + H_z^y \tag{4}$$

and different magnetic ($\sigma^*$) and electric ($\sigma$) conductivities are then assigned to each of the split components in the following manner:

$$\sigma_x^* \leftrightarrow H_x^y, H_x^z \tag{5}$$
$$\sigma_y^* \leftrightarrow H_y^x, H_y^z \tag{6}$$
$$\sigma_z^* \leftrightarrow H_z^x, H_z^y \tag{7}$$
$$\sigma_x \leftrightarrow E_x^y, E_x^z \tag{8}$$
$$\sigma_y \leftrightarrow E_y^x, E_y^z \tag{9}$$
$$\sigma_z \leftrightarrow E_z^x, E_z^y. \tag{10}$$

Maxwell's two curl equations with the above modifications yield 12 differential equations. Below we list four of these

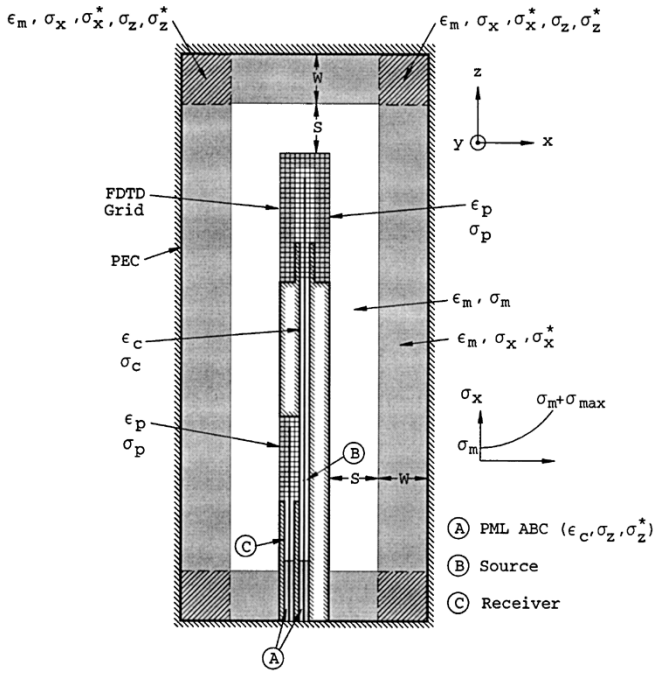


Fig. 3. Two-dimensional cut through the center of the 3-D FDTD model of the probe showing the coaxial cables, antennas, caps, and the PML regions.

equations corresponding to $E_x$ and $H_y$:

$$\epsilon\frac{\partial E_y^x}{\partial t}+\sigma_y E_y^x=-\frac{\partial(H_x^z+H_y^z)}{\partial y} \tag{11}$$

$$\epsilon\frac{\partial E_z^x}{\partial t}+\sigma_z E_z^x=\frac{\partial(H_x^y+H_z^y)}{\partial z} \tag{12}$$

$$\mu\frac{\partial H_z^y}{\partial t}+\sigma_z^* H_z^y=-\frac{\partial(E_y^x+E_z^x)}{\partial z} \tag{13}$$

$$\mu\frac{\partial H_x^y}{\partial t}+\sigma_x^* H_x^y=\frac{\partial(E_x^z+E_y^z)}{\partial x}. \tag{14}$$

In the above equations, $\epsilon$ and $\mu$ are those of the material located in the computation space. Using this formulation one can achieve a zero reflection coefficient at the PML layer by enforcing the following condition:

$$\sigma^*=\frac{\sigma\mu}{\epsilon}. \tag{15}$$

However, it is not feasible to mesh an infinite PML in the FDTD method; therefore, a finite PML backed by a perfect electric conductor (PEC) is used. Fig. 3 shows the regions in the FDTD mesh where the different conductivities are specified; $\epsilon_m$ and $\sigma_m$ are the real part of the dielectric constant and the conductivity, respectively, of the material being measured.

We use a PML layer having a dielectric constant $\epsilon=\epsilon_m$ and a conductivity with a parabolic profile that increases from $\sigma_m$ at the PML interface to $\sigma_m+\sigma_{\max}$ at the PEC wall that terminates the PML. The parabolic profile, as opposed to a constant conductivity profile, serves to reduce the numerical reflection from the discontinuity in the conductivity at the onset of the PML and to attenuate the wave traveling in the PML so that the reflection from the PEC is minimized. Inside

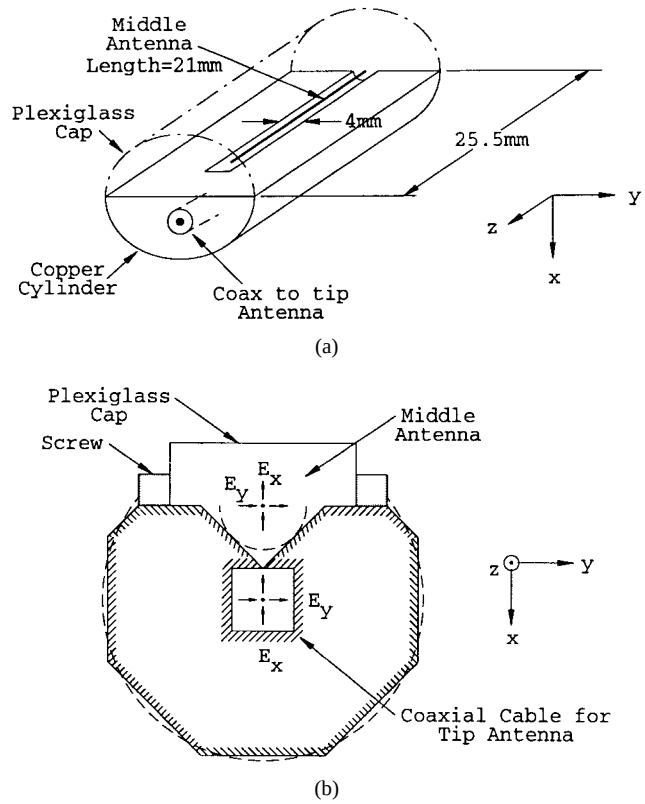


Fig. 4. Detailed geometry near middle antenna. (a) Three-dimensional plot of the middle antenna's geometry. (b) Two-dimensional view of the FDTD model showing the cylinder, cap, screws, slot, and coaxial cable.

the PML's that are orthogonal to the $x$ axis we specify $\sigma_x$ as

$$\sigma_x^i=\sigma_{\max}\left(\frac{i*\Delta x}{W}\right)^2+\sigma_m \tag{16}$$

where $\sigma_{\max}=4.0$ Mho/m, $W=13\times\Delta x=0.0195$ m (width of the PML layer) and $i$ goes from 1 to 13 with $i=1$ corresponding to the first cell in the PML layer. Similar expressions for $\sigma_y$ and $\sigma_z$ are used inside the PML's orthogonal to the $y$ and $z$ axes, respectively.

Due to the presence of the PEC and the discrete implementation of the conductivity profile on the computer, there is present a small reflection from the PML that is on the order of $-50$ dB or less. The PML is placed ten cells away from the probe. The placement of the PML at this distance from the probe did not have an effect on the received signal as found by moving the PML to a distance of 20 cells and comparing the received signals for the 10 and 20 cells separations in free-space. The free-space case is the worst-case situation since for $\sigma_m$ different from zero the wave will be attenuated further before reaching the PML. This low interaction between the PML layer and the probe is due to the fact that the fields around the probe decay as the inverse of the distance from the probe and, therefore, have a low value at the PML.

Both coaxial cables are also terminated with a PML ABC to absorb the waves propagating in the negative $z$ direction (Fig. 3). In the transmit cable these are caused by the wave reflected from the antenna at the end of the transmit cable and in the receive cable by the wave coupled from the tip antenna.

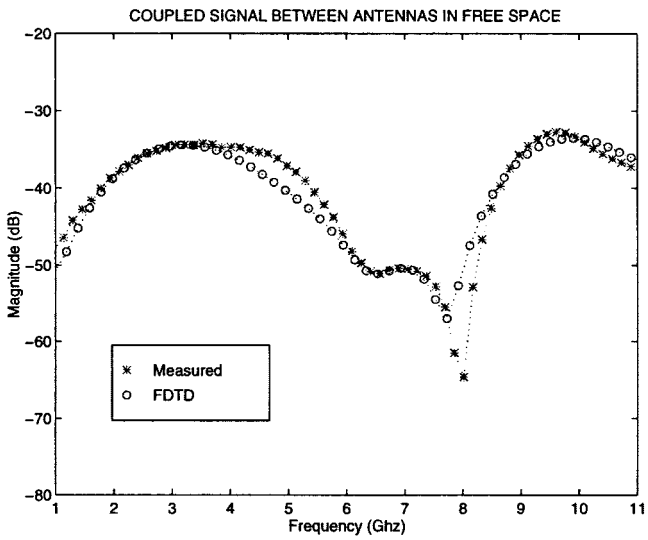


Fig. 5. The transmission coefficient ($S_{21}$) between the probe antennas with free-space as the surrounding medium, measured, and FDTD results.

The conductivity profile for the PML ABC in the cables is also parabolic with $\sigma_{\max} = 2.0$ Mho/m and $W = 30 \times \Delta x = 0.045$ m.

### B. Numerical Results

The coaxial cable radius is 0.15 cm and the cells are chosen to be cubic with their sides being of length 0.15 cm in order to match the radius of the coaxial cables and to model the fine geometrical details of the probe. The space step is one twentieth of a wavelength at 10 GHz. The meshed domain is $60 \times 60 \times 160$ cells. The time-step $\Delta t$ is computed according to the Courant stability condition for the 3-D FDTD algorithm. We choose $\Delta t = 2.0$ ps; the differential equations are then discretized based on the Yee algorithm and the FDTD code is run for 1800 time steps giving a total running time of 3.64 ns. The memory storage required is 78 MB and the CPU time for one code run is 1.7 h on the SGI R4000 workstation.

To compute the transmission coefficient ($S_{21}$) between the antennas the received signal is Fourier transformed to the frequency domain and divided by the source pulse in the transmit cable

$$S_{21} = \frac{\mathrm{FFT}(V_{\mathrm{received}})}{\mathrm{FFT}(V_{\mathrm{source}})}. \tag{17}$$

The computed and measured transmission coefficients ($S_{21}$) between the probe antennas for the case where the surrounding medium is free-space are shown in Fig. 5. The measured and computed data agree very well over the whole frequency range except at the sharp null at 8 GHz. The nulls and peaks in the waveforms are caused by the resonant behavior of the stub antennas. The null at 8 GHz was found to produce some uncertainty in determining the exact attenuation and phase shift at the location of the null. One can reduce its effect considerably by making the slot at the middle antenna wider and using stub antennas with different lengths so as to stagger their resonant frequencies. These changes are being implemented in a second version of the probe. As mentioned earlier the coupling between the antennas for frequencies less than 1 GHz is very small.

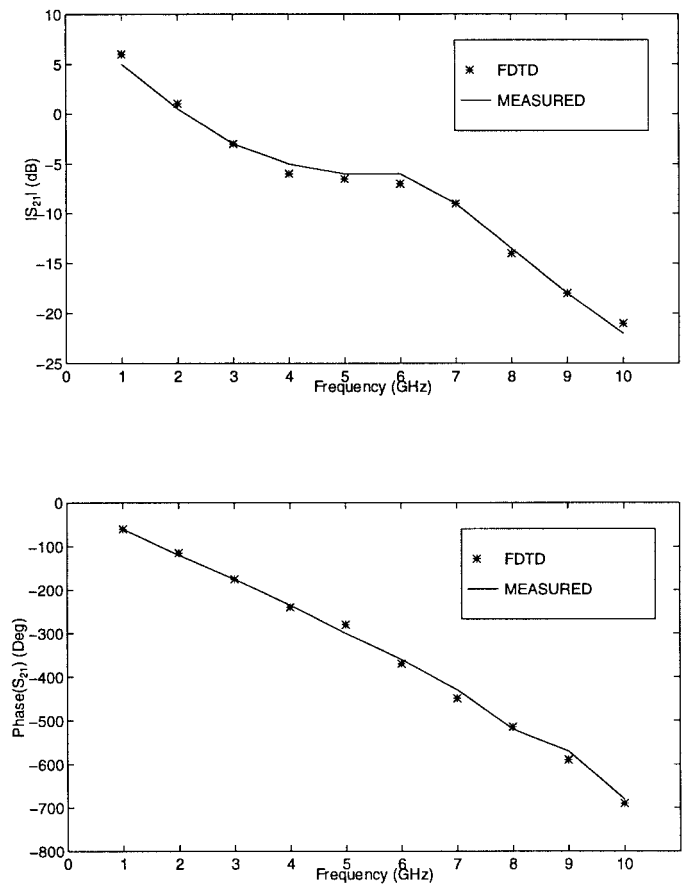


Fig. 6. Measured transmission coefficient ($S_{21}$) in Nylon 66 normalized to that in free-space: (a) the magnitude and (b) the phase. Overlayed are the matching magnitude and phase obtained by running the FDTD code for different $\epsilon_m$ and $\sigma_m$.

## IV. Prediction of Dielectric Constant

In the previous section, we demonstrate that the $S_{21}$ calculations from the FDTD model match the measurements for the probe in free-space. With the validation of the FDTD model, our goal is to demonstrate that the material properties of the surrounding media can be obtained by running the FDTD code for various material parameters until the measurement and calculated data converge. The material parameters of interest are $\epsilon_m$ and $\sigma_m$, where $\epsilon_m$ is the real part of the relative dielectric constant and $\sigma_m$ is related to the relative imaginary part ($\epsilon_r''$) by

$$\sigma_m = 2\pi f \epsilon_r'' \epsilon_0 \tag{18}$$

where $f$ is the frequency.

The first material to be tested is nylon. Measurements are taken from the probe embedded in a large block of Nylon 66. The FDTD model is then run for varying values of $\epsilon_m$ and $\sigma_m$ until the magnitude and phase of $S_{21}$ matches the measurements. Note that the matching is done over the entire frequency range of interest. The magnitude and phase of $S_{21}$ normalized to the $S_{21}$ in free-space are plotted in Fig. 6. The

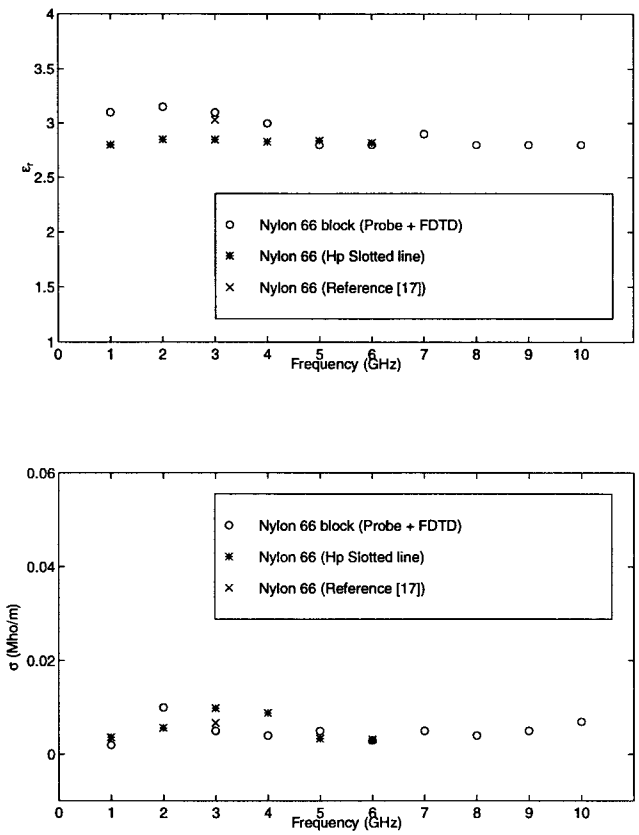


Fig. 7. Dielectric constant and conductivity for Nylon 66 obtained by matching the magnitude and phase of the FDTD results to the measured data. Also shown are the measured dielectric constant and conductivity using a slotted line that operates between 1 and 6 GHz.

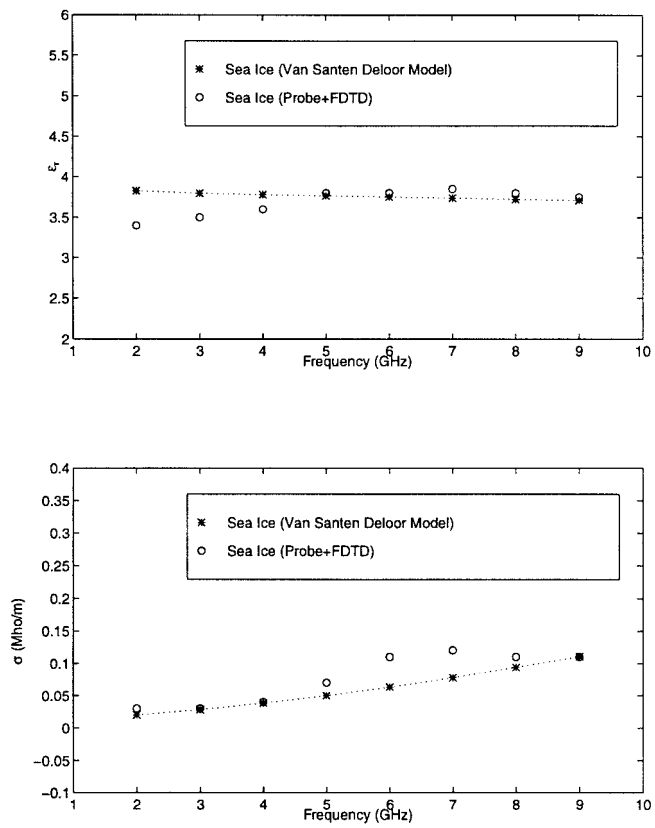


Fig. 8. Dielectric constant and conductivity for sea ice obtained by matching the magnitude and phase of the FDTD results to the measured data. Also shown are the results from the VanSanten DeLoor mixing model.

predicted $\epsilon_m$ and $\sigma_m$ from the probe measurements coupled with the FDTD model are shown in Fig. 7. These results are compared to measurements taken with an HP slotted line device that operates from 1 to 6 GHz [7]. Also shown is the value of the dielectric constant obtained from [17] at a single frequency (3 GHz). This value is consistent with both our measurements and the HP slotted line measurements.

Next we consider the material properties of sea ice. The probe was taken to the Cold Regions Research and Engineering Laboratory (CRREL), where data was obtained from 1 to 9 GHz on a large piece of artificially grown sea ice. The properties of the sea ice grown at the CRREL facility can be carefully controlled and variables such as temperature and salinity are recorded in conjunction with dielectric constant measurements. For the measurement shown here, the temperature of the ice is −4.3 °C with a salinity of 4.0 parts per thousand (ppt). Knowing the temperature and salinity, a dielectric mixing model formulated by Van Santen and Deloor [18], [19], [22] that takes into account the brine inclusions in sea ice can be used to predict the bulk dielectric constant. The brine inclusions are assumed to have ellipsoidal shapes with dimensions obtained from physical observations of sea ice growth [20], [25]. The dimensions of the ellipsoid's three axes are designated by $a, b$, and $c$ and are taken to be 0.4, 0.2, and 1.8 mm, respectively. The relative dielectric constant of pure ice is constant with frequency and equal to $\epsilon_{\text{ice}} = 3.15$. The brine dielectric properties are obtained from Stogryn and Desargeant [21]. This model can be used as a comparison for our probe measurements. As in the case of nylon, the FDTD model is run until the results match the probe measurements. The resulting $\epsilon_m$ and $\sigma_m$ are compared to the dielectric mixing model in Fig. 8. The two plots agree very well for this frequency range; a deviation occurs for the $\sigma$ values in the frequency range between 6–8 GHz, which may be due to the antenna resonance null as mentioned in Section III.

From the above results we see that an accurate prediction of complex dielectric properties can be obtained when the FDTD model is combined with the probe measurement; however, the process of running the FDTD code to match the measurements can be a time-consuming process. An alternative idea is to fully characterize the probe by computing $S_{21}$ for discrete increments of $\epsilon_m$ and $\sigma_m$ at all the frequencies of interest. A lookup table can then be set up which gives the calibrated dielectric constant based on the magnitude and phase of $S_{21}$ and the frequency. Since the data is taken for discrete values of the dielectric property, interpolation must be used to match the measured results to the lookup table. Although not investigated in this study, an optimization routine could be used to minimize the error between the measured and computed $S_{21}$. Because the attenuation of wave between the two antennas is strongly related to $\sigma_m$ and the phase delay between the two antennas is strongly related to $\epsilon_m$, we use the magnitude of $S_{21}$ to interpolate the value of $\sigma_m$ and the phase of $S_{21}$ to interpolate the value of $\epsilon_m$.

TABLE I
A SAMPLE LOOKUP TABLE AT 4 GHz. THE FIRST COLUMN IS THE RELATIVE DIELECTRIC CONSTANT OF THE MATERIAL AND THE FIRST ROW IS THE CONDUCTIVITY OF THE MATERIAL IN Mho/m. EACH TABLE ENTRY SHOWS THE ATTENUATION IN DECIBELS AND THE PHASE DELAY IN DEGREES CORRESPONDING TO $\epsilon_r$ AND $\sigma$

| $\epsilon_r, \sigma$ (Mho/m) | 0.02 | 0.04 | 0.1 | 0.2 | 0.4 |
|---|---|---|---|---|---|
| 2.0 | 5, 130 | 7, 130 | 11, 130 | 18, 120 | 29, 120 |
| 3.0 | 8, 230 | 9, 230 | 12, 220 | 17, 205 | 28, 190 |
| 4.0 | 9, 300 | 10, 300 | 13, 300 | 17, 275 | 26, 260 |
| 5.0 | 9, 370 | 11, 370 | 14, 360 | 16, 340 | 23, 330 |
| 6.0 | 10, 450 | 11, 440 | 12, 410 | 16, 410 | 23, 400 |

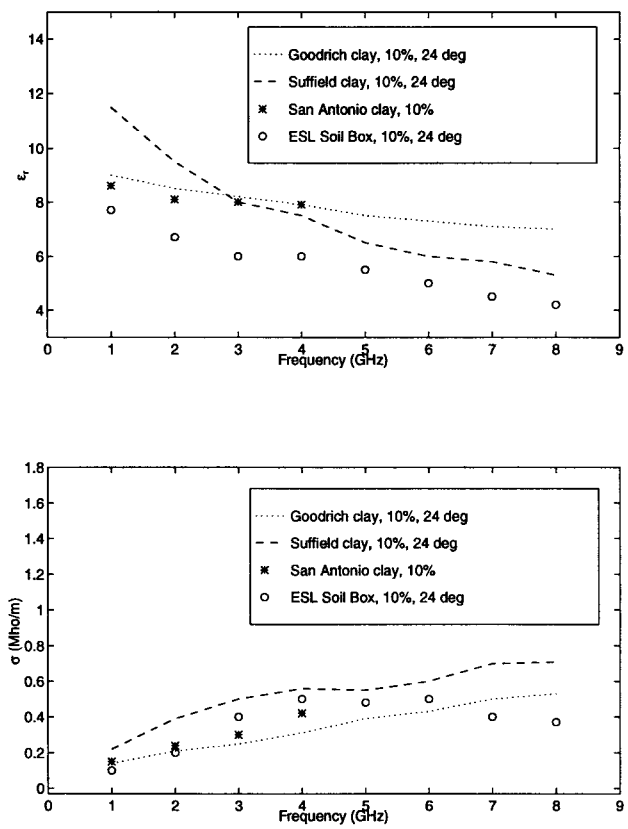


Fig. 9. Dielectric constant and conductivity for soil obtained by matching the magnitude and phase of the FDTD results to the measured data.

A sample table is shown in Table I, which gives the dielectric constant and conductivity values for different attenuation and phase delay at a frequency of 4 GHz.

To demonstrate the capabilities of the lookup table, we consider the case of soil. A sample of soil located in the ElectroScience Lab's (ESL's) soil box, which is used for ground penetrating radar experiments, was measured with the probe. We first attempt to find the dielectric constant values by exactly fitting the measured and computed $S_{21}$ and then by using interpolation between two values obtained from the FDTD model runs. Plots for the dielectric constant values obtained by exactly fitting the measured and computed $S_{21}$ are shown in Fig. 9. Concurrent with the soil measurement we measured the soil moisture, temperature, and density at the

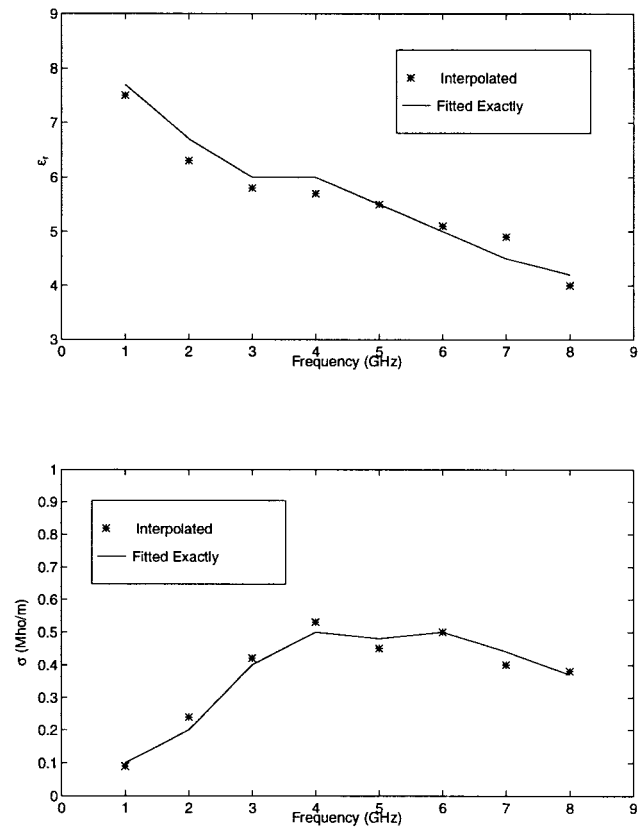


Fig. 10. Dielectric constant and conductivity for soil obtained by interpolating the magnitude and phase of the FDTD results to match the measured data.

location where the probe measurements were taken and used this information to compare with dielectric constant values obtained by other investigators [23], [24]. Given the variability in soil samples from one location to the other even for the same type of soil, we see a very good agreement between the probe measurement and the results from [23] and [24]. By interpolating between the FDTD results at each frequency we obtain the dielectric constant values shown in Fig. 10 where we have overlayed the dielectric constant values from Fig. 9 obtained by exactly fitting the measured data. This comparison demonstrates the feasibility of this approach where we can reduce the computation time by performing fewer FDTD runs.

For all the cases mentioned above, the dielectric constant values obtained with the probe were within 10% of the reference data obtained by independent methods. This process can be generalized for other materials by setting up lookup tables that give the calibrated dielectric constant based on the measured attenuation and phase delay with respect to free-space. Those tables can be generated for each desired frequency and expanded to have a finer resolution and to cover a wider range of values.

## V. CONCLUSION

A new probe for the *in situ* measurement of the complex dielectric constant of materials was presented. The probe operates in the range of frequencies from 1 to 10 GHz and uses two antennas mounted on a cylinder to measure

the transmission coefficient through the material under study. Probe performance was modeled using an FDTD approach. It was found that the FDTD analysis which properly accounts for antenna coupling and medium effects on antenna impedance was necessary to obtain $\sigma$ and $\epsilon$ with an accuracy of better than plus or minus 10%. After calibration with respect to the transmission coefficient in free-space, the attenuation and phase delay of the signal in the material are compared to the values obtained from a numerical model of the probe in order to predict the complex dielectric constant. The probe was found to be a useful tool for the *in situ* measurement of the dielectric constant as shown by measurements done on a sample of nylon and on soil and sea ice. The probe design principles discussed here could be used for other operating frequencies by scaling the stub antenna sizes and distances as mentioned in Section III, the side antenna gap and shape should be modified in next generation probes, regardless of operating frequency. Applications that take advantage of this device range from ground penetrating radar to remote sensing of land and vegetation where knowledge of the dielectric constant can prove crucial to the interpretation of the radar backscatter data.

## ACKNOWLEDGMENT

The authors would like to thank Prof. K. Jezek of the Byrd Polar Research Center, The Ohio State University, Columbus, for providing the sea ice measurements.

## REFERENCES

[1] M. N. Afsar, J. R. Birch, and R. N. Clarke, "The measurement of the properties of materials," *Proc. IEEE*, vol. 74, pp. 183–199, Jan. 1986.

[2] M. R. Vant, R. O. Ramseir, and V. Makios, "The complex dielectric constant of sea ice at frequencies in the range 0.1 to 40 GHz," *J. Appl. Phys.*, vol. 49, pp. 1264–1280, Mar. 1978.

[3] "IEEE guide for radio methods of measuring earth conductivity," IEEE Std. 356-1974, pp. 375–391, 1974.

[4] P. Hayes, "A single-probe on-site method of measuring the dielectric constant and conductivity of soft earth media over a 1-GHz bandwidth," *IEEE Trans. Geosci. Remote Sensing*, vol. GRS-20, pp. 504–510, Oct. 1982.

[5] J. D. Kraus, *Antennas*, 2nd ed. New York: McGraw-Hill, 1988.

[6] J. A. Stratton, *Electromagnetic Theory.* New York: McGraw-Hill, 1941, pp. 527–531.

[7] J. R. J. Gau and W. D. Burnside, "Dielectric constant measurement using a slotted line with comparison of reflection and transmission methods," ElectroSci. Lab., Dept. Elect. En., The Ohio State Univ., Columbus, OH, Tech. Rep. 727723-2, June 1994.

[8] R. E. Collin, *Foundations for Microwave Engineering.* New York: McGraw-Hill, 1966.

[9] K. S. Yee, "Numerical solution of initial boundary value problems involving Maxwell's equations in isotropic media," *IEEE Trans. Antennas Propagat.*, vol. AP-14, pp. 302–307, May 1966.

[10] J. G. Maloney, G. S. Smith, and W. R. Scott, Jr., "Accurate computation of the radiation from simple antennas using the finite-difference time-domain method," *IEEE Trans. Antennas Propagat.*, vol. 38, pp. 1059–1068, July 1990.

[11] R. J. Luebbers and J. Beggs, "FDTD calculation of wide-band antenna gain and efficiency," *IEEE Trans. Antennas Propagat.*, vol. 40, pp. 1403–1407, Nov. 1992.

[12] M. Jensen and Y. Rahmat-Samii, "Performance analysis of antennas for hand-held transceivers using FDTD," *IEEE Trans. Antennas Propagat.*, vol. 42, pp. 1106–1113, Aug. 1994.

[13] A. Taflove, K. R. Umashankar, B. Beker, F. Harfoush, and K. S. Yee, "Detailed FD-TD analysis of electromagnetic fields penetrating narrow slots and lapped joints in thick conducting screens," *IEEE Trans. Antennas Propagat.*, vol. 36, pp. 247–257, Feb. 1988.

[14] R. Lee and T. T. Chia, "Analysis of electromagnetic scattering from a cavity with a complex termination by means of a hybrid ray-FDTD method, " *IEEE Trans. Antennas Propagat.*, vol. 41, pp. 1560–1569, Nov. 1993.

[15] J. P. Berenger, "A perfectly matched layer for the absorption of electromagnetic waves," *J. Comp. Phys.*, vol. 114, no. 2, pp. 185–200, Oct. 1994.

[16] W. C. Chew and W. H. Weedon, "A 3-D perfectly matched medium from modified Maxwell's equations with stretched coordinates," *Microwave Opt. Technol. Lett.*, vol. 7, no. 13, pp. 599–604, Sept. 1994.

[17] R. F. Harrington, *Time Harmonic Electromagnetic Fields.* New York: McGraw-Hill, 1961, p. 453.

[18] D. Polder and J. H. VanSanten, "The effective permeability of mixtures of solids," *Physica*, vol. 12, no. 5, pp. 257–271, Aug. 1940.

[19] G. P. De Loor, "Dielectric properties of heterogeneous mixtures containing water," *J. Microwave Power*, vol. 3, pp. 67–73, 1968.

[20] A. J. Gow, S. A. Arcone, and S. G. McGrew, "Microwave and structural properties of saline ice," CRREL Rep. 87-20, Oct. 1987.

[21] A. Stogryn and C. J. Desargeant, "The dielectric properties of brine in sea ice at microwave frequencies," *IEEE Trans. Antennas Propagat.*, vol. AP-33, pp. 523–532, May 1985.

[22] G. F. N. Cox and W. F. Weeks, "Equations for determining the gas and brine volumes in sea ice samples," *J. Glaciol.*, vol. 29, no. 102, pp. 306–316, 1983.

[23] J. E. Hipp, "Electromagnetic parameters as functions of frequency, soil density and soil moisture," *Proc. IEEE*, vol. 62, pp. 98–103, Jan. 1974.

[24] P. Hoekstra and A. Delaney, "Dielectric properties of soils at UHF and microwave frequencies," *J. Geophys.*, vol. 79, no. 11, pp. 1699–1708, Apr. 1974.

[25] E. M. Nassar, R. Lee, K. Jezek, and J. D. Young, "*In situ* measurement of the complex dielectric constant of sea ice from 1 to 10 GHz," *Int. Geosci. Remote Sensing Symp.*, Lincoln, NE, May 1996, pp. 180–182.

[26] E. M. Nassar, R. Lee, and J. D. Young, "Electromagnetic probe for *in situ* measurement of the complex dielectric constant of materials," in *IEEE AP-S Int. Symp. URSI Meet. Dig.*, Baltimore, MD, July 1996, p. 158.

**Elias M. Nassar** (S'90–M'98) received the B.E. degree in electrical engineering (with distinction) from the American University, Beirut, Lebanon, in 1990, and the M.S. and Ph.D. degrees in electrical engineering from The Ohio State University, Columbus, OH, in 1992 and 1997, respectively.

From 1990 to 1997, he was a Graduate Research Assistant at the ElectroScience Laboratory, The Ohio State University, where he worked on numerical modeling and testing of antennas for ground penetrating radar and remote sensing of sea ice. In 1997 he was employed as a Graduate Teaching Assistant in the Electrical Engineering Department, The Ohio State University, where he taught laboratory courses. In 1998 he joined the faculty of the Electrical and Computer Engineering Department, Notre Dame University, Lebanon, as an Assistant Professor. His current research interests include the use of numerical methods in electromagnetics to model antennas for mobile communications and radar remote sensing and developing novel methods in engineering.

**Robert Lee** (S'82–M'90) received the B.S.E.E. degree in 1983 from Lehigh University, Bethlehem, PA, and the M.S.E.E. and Ph.D. degrees from the University of Arizona, Tucson, in 1988 and 1990, respectively.

From 1983 to 1984, he worked for Microwave Semiconductor Corporation, Somerset, NJ, as a Microwave Engineer. From 1984 to 1986 he was a Technical Staff Member at Hughes Aircraft Company, Tucson, AZ. From 1986 to 1990 he was a Research Assistant at the University of Arizona. In addition, during the summers of 1987 through 1989 he worked at Sandia National Laboratories, Albuquerque, NM. Since 1990 he has been at The Ohio State University, Columbus, where he is currently an Associate Professor. His main research interest is in the analysis and development of finite methods for electromagnetics.

Dr. Lee's is a member of the International Union of Radio Science (URSI).

**Jonathan D. Young** (M'71–SM'93–F'98) was born in Dayton, OH, on June 29, 1941. He received the B.S.E.E. (*summa cum laude*), M.Sc., and Ph.D. degrees from The Ohio State University, Columbus, in 1964, 1965, and 1971, respectively.

He has been a professional Researcher and Project Principal Investigator at the ElectroScience Laboratory (ESL), The Ohio State University, from 1971 to the present, and Associate Director of ESL from 1984 to the present. He has more than 25 years experience in ground penetrating radar. He developed and holds patents on the Terrascan buried utility locator, which won an IR100 award from Industrial Research Magazine in 1978. His recent ground penetrating radar (GPR) research is devoted to improved antennas, airborne GPR systems, and unexploded ordnance detection and identification. He has performed research studies on ultrawide-band (UWB) scattering of airborne and surface targets. His project developed the Ohio State University compact radar cross-section range, which obtains 1–96 GHz UWB scattering signatures. His recent involvement in transient scattering phenomenology studies involve higher order scattering mechanisms in target signatures and in the application of radar image processing to extract these features. He has studied foliage penetrating radar propagation, clutter, and target scattering phenomenology. He created UWB coherent synthetic array radar (SAR) images of targets in a forest for the ARPA BTI study concerning UWB radar. He has recently developed new techniques for development and specification of radar antenna performance for this application. Most recently, he has been developing techniques for look-ahead radar guidance of vehicles, associated with automated highway system studies. He is Co-Inventor of the frequency selective surface highway stripe. He led the development of the radar system to implement automated radar steering in an automobile, which was demonstrated at the 1997 Automated Highway System demo in San Diego, CA.